

Continuum and Quantum-Chemical Modeling of Oxygen Reduction on the Cathode in a Solid Oxide Fuel Cell

YongMan Choi · David S. Mebane ·
Jeng-Han Wang · Meilin Liu

Published online: 28 November 2007
© Springer Science+Business Media, LLC 2007

Abstract Solid oxide fuel cells (SOFCs) have several advantages over other types of fuel cells such as high-energy efficiency and excellent fuel flexibility. To be economically competitive, however, new materials with extraordinary transport and catalytic properties must be developed to dramatically improve the performance while reducing the cost. This article reviews recent advancements in understanding oxygen reduction on various cathode materials using phenomenological and quantum chemical approaches in order to develop novel cathode materials with high catalytic activity toward oxygen reduction. We summarize a variety of results relevant to understanding the interactions between O_2 and cathode materials at the molecular level as predicted using quantum-chemical calculations and probed using in situ surface vibrational spectroscopy. It is hoped that this in-depth understanding may provide useful insights into the design of novel cathode materials for a new generation of SOFCs.

Keywords Solid oxide fuel cells · Oxygen reduction · Continuum modeling · Quantum-chemical calculations

1 Introduction

The search for clean, secure, and sustainable energy technologies has stimulated great interest in fuel cells [1]. According to the electrolyte materials used, fuel cells are classified into

solid oxide fuel cell (SOFC), molten carbonate fuel cell (MCFC), phosphoric acid fuel cell (PAFC), polymer electrolyte membrane fuel cell (PEMFC), and alkaline fuel cell (AFC) [2]. Among all types of fuel cells, SOFCs have attracted much attention because of several advantages over other types of fuel cells, including high-energy efficiency (especially when combined with turbines) and excellent fuel flexibility (offering the possibility for direct utilization of hydrocarbon fuels, biomass, and other renewable fuels) [2–9]. As Singh and Minh pointed out [8], numerous improvements in SOFC materials (including cathode, anode, current-collector, and sealant) have been made under the DOE-NETL-SECA (Solid State Energy Conversion Alliance) core technology program [10] since 1999. Steele [2] emphasized that development of cost-effective fuel-cell materials plays a pivotal role in market entry to compete with conventional energy technology—US DOE/SECA's target is \$400/kW [8, 10].

It is well known that several technical challenges have to be overcome to commercialize SOFC technology, including coking and sulfur poisoning of the anode (for direct utilization of hydrocarbon fuels), chromia poisoning of the cathode (due to Cr-containing cell components such as the interconnect), and reducing the operating temperature to the range where much less expensive materials may be used as cell components [3, 8, 11, 12]. As the operating temperature is lowered, however, the polarization due to oxygen reduction at the cathode represents a significant internal loss in SOFC operation [11]. Thus, the design of novel cathode materials with high catalytic activity for oxygen reduction at low temperatures is a critical step toward low-cost SOFCs. To date, however, our understanding of the mechanisms and kinetics of oxygen reduction under fuel cell operating conditions remains incomplete because of the complexity of the electrochemically active interfaces.

Y. Choi · D. S. Mebane · J.-H. Wang · M. Liu (✉)
Center for Innovative Fuel Cell and Battery Technologies,
School of Materials Science and Engineering,
Georgia Institute of Technology, Atlanta,
GA 30332, USA
e-mail: meilin.liu@mse.gatech.edu

As schematically illustrated in Fig. 1, the electrochemical reduction of oxygen is composed of various elementary steps and one of the key challenges is to sort out the reaction sequence and identify the rate-limiting steps [13, 14]. Microscopic modeling techniques, such as quantum-chemical calculations, are becoming more widely recognized as a useful complement for experiments in our efforts to obtain a suitable picture of the cathode processes. This article reviews the current status of research into the oxygen reduction reaction at cathode materials in SOFCs at the macro and microscopic levels. Then, we will emphasize the promising application of quantum-chemical calculations for better understanding of the cathode reaction and in rational design of novel cathode materials for SOFCs. In the process, we will highlight a few significant areas that can provide insights into the development of better cathode materials.

2 Current Status of the Overall Oxygen Reduction Picture

The phenomenology of oxygen reduction on the cathode of an SOFC has been discussed in detail elsewhere [13, 15, 16]. Shown in Fig. 2 are some of the possible pathways for oxygen reduction at cathode surfaces, electrolyte surfaces, and triple-phase boundaries (TPBs)—where a cathode, an electrolyte, and gaseous oxygen molecules meet. The surfaces of an electrolyte or a cathode are considered two-phase boundary (2PB) areas whereas the TPBs are considered to be lines, although they may broaden to a zone due to transport along surfaces of the adsorbed oxygen species (O_2 , O_2^- , O_2^{2-} , and O^-) and electronic species (e' and h^\bullet).

Dominating the mechanism of oxygen reduction is the role of the cathode material, typically a mixed ionic-electronic conductor (MIEC, a material conductive to both ionic and electronic species), and its relationship to the gas and the electrolyte. Serving the purpose of establishing some general principles of oxygen reduction on MIECs, this section will concisely review the most popular MIECs

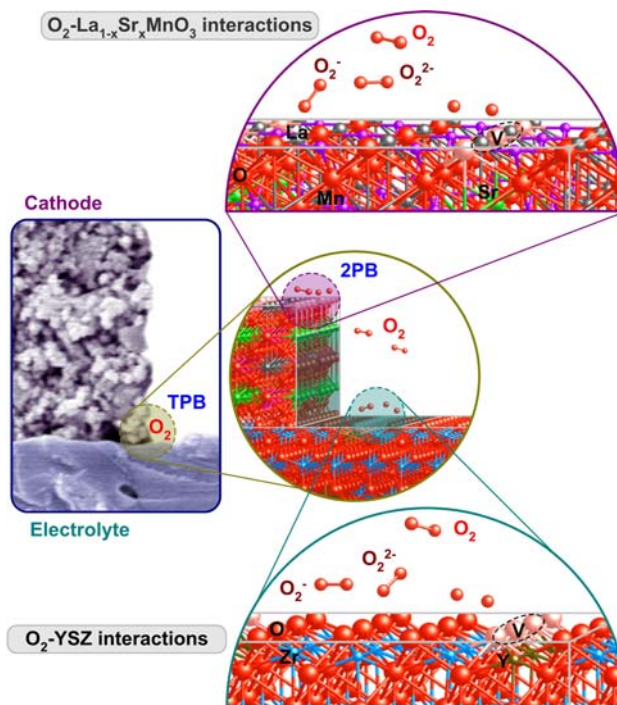


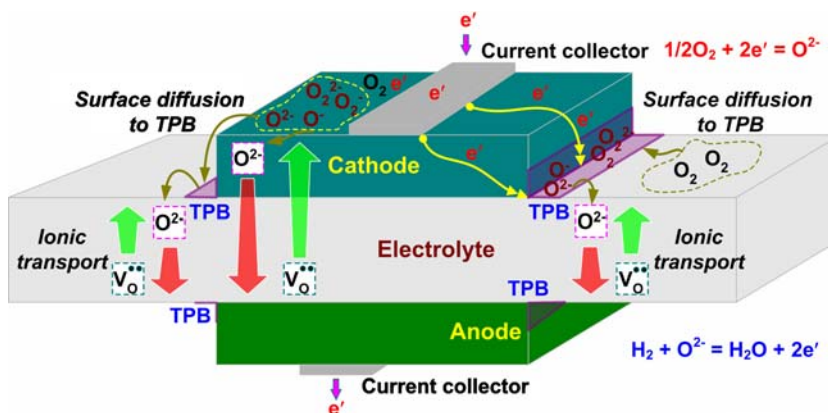
Fig. 2 Possible pathways for oxygen reduction on the cathode in an SOFC

for SOFC cathode applications, the perovskites $La_{0.8}Sr_{0.2}MnO_{3 \pm \delta}$ (LSM) and $La_xSr_{1-x}Co_yFe_{1-y}O_{3-\delta}$ (LSCF). The treatment of LSCF does not continue in subsequent sections of the paper, but for general understanding, it provides a good contrast to LSM, a material showing complex catalytic behavior which is nonetheless the material of most significant engineering importance for SOFC cathodes.

2.1 General Knowledge

LSM and LSCF share a similar crystal structure, and are both p -type electronic and oxygen ion conductors.

Fig. 1 Schematic of oxygen reduction and the relevant transport processes in an SOFC



The primary difference between LSM and LSCF is conductivity: LSCF shows a much higher electronic and ionic conductivity than LSM. Despite this, LSM remains the dominant cathode material for SOFCs, due to its better chemical and thermal compatibility with the dominant electrolyte (YSZ).

The overall reaction for a *p*-type, oxygen-conducting SOFC cathode can be described as



where, in the Kröger-Vink notation, $\text{V}_{\text{O}}^{\bullet\bullet}$ denotes an oxygen vacancy in the solid state (either in the electrolyte or in the MIEC) with two effective positive charges (with respect to the perfect crystal), $\text{O}_{\text{O}}^{\times}$ denotes a neutral oxygen ion in a solid state oxygen site, and h^{\bullet} denotes a positively charged electron hole. However, as mentioned in the introduction to this section, the reaction divides into several elementary steps, including:

- adsorption of gaseous molecular oxygen
- reduction and dissociation of the adsorbed molecule in (probably) multiple steps
- diffusion of adsorbates to various incorporation sites on the MIEC surface and at the TPB
- transport of vacancies to the incorporation sites
- transport of electron holes away from the reduction sites
- the incorporation reaction (combination of adsorbed atomic oxygen and oxygen vacancies)

and

- the diffusion of vacancies from the electrolyte into the MIEC.

Researchers have begun to untangle all of these steps, but knowledge is especially short on the sequence and kinetics of reactions at the air-exposed surface.

Early electrochemical experiments focused on drawing distinctions between bulk-mediated (involving diffusion of oxygen through a bulk phase) and surface-mediated (diffusion of oxygen across a surface) processes in reaction (1). Experiments on LSM thin films showed a linear thickness dependence for the electrode resistance, suggesting a bulk-mediated process [17–21]. However, experiments on porous electrodes or cracked films suggest that resistances in LSM frequently scale with the TPB length, with lower resistances than their dense-film counterparts [20, 22, 23]. This leads to the conclusion that, when available, a surface-mediated mechanism will dominate in LSM. For LSCF, the bulk-mediated view seems relatively secure [24, 25].

The parallel paths of surface and bulk in LSM greatly complicate our ability to get a quantitative grip on the reaction mechanism. Moreover, LSM displays a decreased

electrode resistance at high cathodic potentials or after extended cathodic polarization [20, 26, 27]. Although it is still under study, this phenomenon may reflect changes in cathode surface structure [28–30].

Independent measurements of defect concentrations led to classical thermodynamic and physical models for defect equilibria in both LSM and LSCF [31–36]. The oxygen nonstoichiometry data available for LSCF is more reliable than that for LSM, because of the much higher concentration of oxygen vacancies in LSCF. Defect models for LSM may still be considered somewhat incomplete for this reason. Given the high electronic transference numbers of both materials, electronic measurements such as the four-point probe and thermoelectricity create greater confidence in electronic structure and transport models, which generally depict a hopping mechanism involving e_g and t_{2g} energy levels of the Mn ion in LSM [34, 37, 38], and a band conduction model for LSCF.

Techniques for measuring surface exchange and ionic diffusivity in LSM and LSCF include electron blocking, current interrupt, and isotope exchange/secondary ion mass spectroscopy (SIMS) [39–50]. But because the overall rate law for the surface reaction is likely nonlinear, and the rate laws for elementary steps depend exponentially on the surface potential, this limits the utility of average measurements to small perturbations from equilibrium. In addition, both surface exchange and diffusion constants for oxygen seem to depend on the vacancy concentration [46], which, as mentioned, is difficult to measure in LSM.

2.2 Quantitative Continuum Modeling

2.2.1 One-Dimensional Models and Porous Electrode Theory

Treatments of a one-dimensional, homogeneous medium with multiple charged species using the Nernst-Planck and Poisson equations date back decades. Brumleve and Buck numerically solved the full nonlinear problem in one dimension in 1978 [51]. Recently, it became more popular to follow Brumleve's alternate approach of treating the linearized problem (which is appropriate for low-signal experiments such as impedance spectroscopy) using an "exact" equivalent circuit [52]. Many of the resulting transmission-line circuits apply to MIECs [53, 54]. These approaches are appropriate for thin films with truly one-dimensional symmetry, implying the literal absence of multi-dimensional effects at the continuum scale.

The most popular modeling technique for MIECs appearing in the literature relies on porous electrode theory [55–60], as initially developed for porous electrodes submerged in liquid electrolytes. In the context of SOFC

electrodes, this approach reduces a porous material to a monolithic continuum, with the reactions at the internal surfaces treated as homogeneous reactions within the system. Combined with an assumption of infinite electronic mobility (not a bad assumption for macroscopic LSM or LSCF) symmetry considerations permit a reduction of the problem domain to one dimension. A handful of other simplifications and linearization of the resulting equations (for impedance spectroscopy) enables an analytical solution. Nonlinear results follow from standard, easily implemented finite difference methods and regression solvers [61].

One prominent application of this technique focused on porous MIECs of high ionic conductivity such as LSCF, assuming no surface diffusion of adsorbed oxygen [56]. Simulated impedance spectra matched experimental results, providing a strong argument for the dominance of the bulk pathway in such materials [24, 56]. The transmission-line model also achieved some success in comparison of experiment and model for LSCF, using circular microelectrodes [25, 54].

Models for LSM cannot generally ignore surface diffusion. Several porous electrode models considered both bulk and surface transport in LSM, leaving equations in nonlinear form and solving through finite difference discretizations [55, 57–59]. One such model produced an interesting result in accordance with experimental evidence, showing that, in a relatively poor ionic conductor such as LSM, the reduction process may gradually shift from surface-mediated toward a more active bulk with increasingly negative applied potential [55]. It is generally recognized that this shift is due to the increasing reduction of the bulk under cathodic polarization, yielding a higher concentration of vacancies in the bulk, which aids both transport and surface reaction kinetics.

Despite their success in advancing understanding of basic reduction mechanisms, porous electrode theory and other one-dimensional models are probably not the best vehicles for moving forward with consideration of reactions at the air-exposed surface. The principal difficulty is the limitation in terms of model geometry; of course, porous electrode theory requires a porous electrode for homogenization purposes, and such electrodes are notoriously difficult to characterize microstructurally. Also, one-dimensional modeling regimes will not suffice for any geometry engendering multi-dimensional effects, as is the case with many composites, patterned electrodes and thin films appropriate for fundamental investigation in LSM.

2.2.2 Multi-Dimensional Simulations

A few multi-dimensional simulations of SOFC cathodes which appeared over the past few years [62–65] illustrated

the benefits of expanding the model dimensionality. For example, each MIEC is characterized by ionic diffusion lengths, determined by the chemical surface kinetics and transport properties of the MIEC. When these lengths fall below the particle size in a porous electrode, only multi-dimensional simulations that account for the particle shape are capable of accurately modeling the species flux [13, 65]. Also, multi-dimensional simulations can model current constriction due to linear features such as grain boundaries and TPBs [63].

Muti-dimensional simulations can also treat sheet resistance effects, which can be especially important for thin films suitable for investigation of surface reactions. Experiments on patterned electrodes demonstrated the limitation of the assumption of infinite electronic mobility in LSM [66, 67]. Recently a two-dimensional model for thin-film electrodes was developed that discards this assumption [68]. The simulation successfully replicated the sheet resistance-oriented behavior seen in steady-state DC measurements on thin LSM films [17, 19, 21].

3 Quantum-Chemical Modeling of the Cathode Reaction in SOFCs

While investigations into oxygen reduction on the cathode of an SOFC using electrochemical techniques have provided useful information in selection of cathode materials and in preliminary design and optimization of cathode microstructures, they offer little information about the mechanism of oxygen reduction [11]. The application of in situ Fourier Transform Infrared (FTIR) and Raman micro-spectroscopy [69–71] has revealed some useful information on the mechanism of oxygen reduction; however, they are still unable to probe many mechanistic details due to the complexity of surface processes. For example, experimental measurements to date are still unable to identify the active sites for oxygen reduction at cathode surfaces, especially for perovskite ABO_3 materials. In this section, we will review the latest developments in understanding the electronic structures of several cathode materials as well as the potential energy surfaces (PESs) of elementary reaction steps for oxygen reduction on these materials, as predicted by quantum-chemical calculations. Detailed understanding of reaction mechanisms is imperative to achieving rational design of more efficient SOFC cathode materials [72].

3.1 Quantum-Chemical Methods

Rapid advances in computation make it possible to realistically simulate bulk and surface properties of many

catalytically active materials using computational techniques based on quantum chemistry [73–82], including atomic- and molecular-electronic structures, geometrical parameters, and energetic information of bulk and surface reactions. With proper thermodynamic corrections to take into consideration the effect of temperature and pressure, quantum-chemical calculations can be used to estimate thermodynamic properties, reaction kinetics, and reaction mechanisms which are difficult to measure experimentally.

Quantum chemistry applies quantum mechanics to calculate chemical information [83]. Detailed mathematical methods and approximations related to quantum-chemical calculations can be found in various quantum chemistry text books [83–85] and theoretical descriptions in solids are dealt in Harrison's book [86]. In addition, much information on computational chemistry, from basic concepts to theoretical methods with a lot of examples, is covered by Szabo and Ostlund [87] and Jensen [88].

Typically, the time-independent Schrödinger equation is sufficient to obtain the required information for reaction systems such as optimized geometries and energetics [83–85].

$$\hat{H}\Psi = E\Psi \quad (2)$$

where, the Hamiltonian \hat{H} is an operator corresponding to the sum of kinetic (\hat{T}) and potential (\hat{V}) energy, Ψ the wave function, and E the total energy of the system. The operators \hat{T} and \hat{V} [89] are given by

$$\hat{T} = -\frac{\hbar}{8\pi^2} \sum_i \frac{1}{m_i} \left(\frac{\partial^2}{\partial x_i^2} + \frac{\partial^2}{\partial y_i^2} + \frac{\partial^2}{\partial z_i^2} \right) \quad (3)$$

$$\hat{V} = \sum_{i < j} \sum \frac{e_i e_j}{r_{ij}} \quad (4)$$

where, m , \hbar , e and r_{ij} denote the mass of the particle, Planck's constant, electric charge, and the distance between particles i and j , respectively. It is well known that only one electron systems such as H_2^+ can be exactly solved [88]. However, solving the Schrödinger equation for many body systems such as surface reactions is possible by simplifying with the adiabatic or Born-Oppenheimer approximation [90, 91] for separating the motion of nuclei and electrons. We may categorize quantum chemical approaches into semi-empirical and ab initio methods [82, 83, 92] (e.g., neglect of differential diatomic overlap (NDDO) integral approximation [93] or the Hartree-Fock (HF) model [94–96], respectively). While the semi-empirical methods are derived from available experimental results, ab initio approaches do not rely on experimental data [83]. Thus, ab initio calculations are also called first-principles calculations. Even though a lot of approaches such as Møller-Plesset perturbation theory [88, 97] (MP n , $n = 2, 3, 4$, or higher), Coupled Cluster (CI) approaches

[98], and Complete Active Space Multiconfiguration SCF (CAS-SCF) [99] have been introduced to improve the physical accuracy of ab initio methods, they are still limited to small chemical systems.

Density functional theory (DFT) [100] has been extensively used since the DFT method requires less computational time, but provides a high accuracy in geometrical parameters, binding energies, and vibrational frequencies [91], allowing more practical calculations in surface chemistry related problems [82, 91, 101]. Ab initio methods first solve the Schrödinger equation to obtain the wave function (Ψ) and then the electron density (ρ) as described, while the DFT approach calculates the electron density and then predicts other properties [83]. This means that the energy of the ground state depends on the electron density, $E_0 = E_0[\rho]$, as introduced by Hohenberg and Kohn [102]. According to the Kohn-Sham orbital [100, 102], the ground-state energy can be expressed as follows:

$$E_0[\rho] = T[\rho] + \langle E_{N-E}[\rho] + E_{E-E}[\rho] + E_{N-N}[\rho] \rangle + E_{xc}[\rho] \quad (5)$$

where, T , N , E , and E_{xc} denote the kinetic energy, nuclei, electrons, and the exchange-correlation energy, respectively. The second term in the brackets represents the Coulomb energy. (A more detailed derivation appears in [83]). One of the most crucial issues in applying the DFT approach is obtaining reliable exchange-correlation energies expressed by the electron density (ρ) because they are not known for molecules [83]. This is why numerous approximations have been introduced such as the local density approximation (LDA) and the generalized gradient approximation (GGA) [83, 88]. For the LDA method, the electron density is assumed as a homogenous electron gas, while the GGA approach considers an inhomogeneous electron gas. Thus, according to the GGA, E_{xc} depends on both the electron density (ρ) and its derivatives [88]. Because the GGA functionals including PW91 [103, 104] and PBE [105] have higher accuracy in geometrical parameters and energetics than the LDA [88], the GGA methods are more frequently used in quantum-chemical calculations, especially in surface science.

Another significant step for gas-surface calculations is the construction of appropriate surface models with high accuracy. It is known that three types of surface models (i.e., cluster, embedding, and periodic slab models) are applicable; however, the cluster and slab models are frequently used in surface science [80, 91, 101, 106]. As illustrated in Fig. 3a, the cluster model (usually with the localized basis set) uses a limited number of atoms and produces quite accurate energetics and molecular parameters. However, Jacob and Goddard III [106] pointed out some unreasonable boundary effects and the necessity of a systematic validation for convergence. In order to avoid the

boundary effects, 2-D slab model (usually with the plane wave) has been widely applied in surface science to study gas-surface interactions at 2PBs, as schematically illustrated in Fig. 3b for the interactions between an SOFC anode, Ni(111), and H₂S-contaminated hydrocarbon fuels [107, 108]. The 2-D surface calculations require a vacuum space (to guarantee no interactions between slabs) and employ periodic boundary conditions (PBCs) [86]. Similarly, illustrated in Fig. 2 is a slab model for oxygen reduction near a juncture between the electrolyte and the electrode, where TPBs have to be considered in addition to the two types of 2PBs.

It is fortunate that a variety of software packages for quantum-chemical calculations are readily available, including GAUSSIAN [109], MOLPRO [110], the General Atomic and Molecular Electronic Structure System (GAMESS) [111], Car-Parrinello Molecular Dynamics (CPMD) [112], and Vienna ab initio simulation package (VASP) [113, 114]. Even though these packages make it more convenient to examine our chemical intuition and ideas, it is still important to choose an appropriate computational method and surface model [88]. Regarding SOFC materials, as depicted in Fig. 2 for TPBs, the cathode materials can be considered an infinite number of atoms at the molecular level. Among the surface models for O₂-surface interactions, the periodic slab-model framework has been applied most frequently in order to avoid the boundary effects of the cluster approach and to mimic cathode materials (or metal oxides) [115–117].

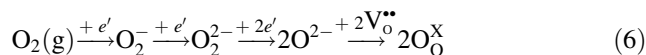
3.2 Investigations into Oxygen Reduction Mechanisms Using Periodic DFT Methods

Oxygen reduction on various cathode materials (metals [118–126] and metal oxides [116]) have been studied using either cluster or periodic slab models. In this section, we

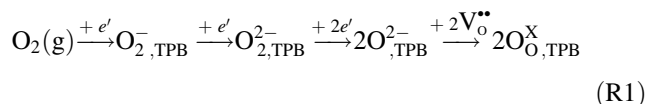
will review DFT calculations of oxygen reduction on electrode and electrolyte surfaces (2PBs and TPBs) to gain more insight into the reaction sequence of oxygen reduction.

3.2.1 Oxygen Reduction on Metallic Surfaces and TPBs

Oxygen reduction on a metallic electrode can be generally described as follows:

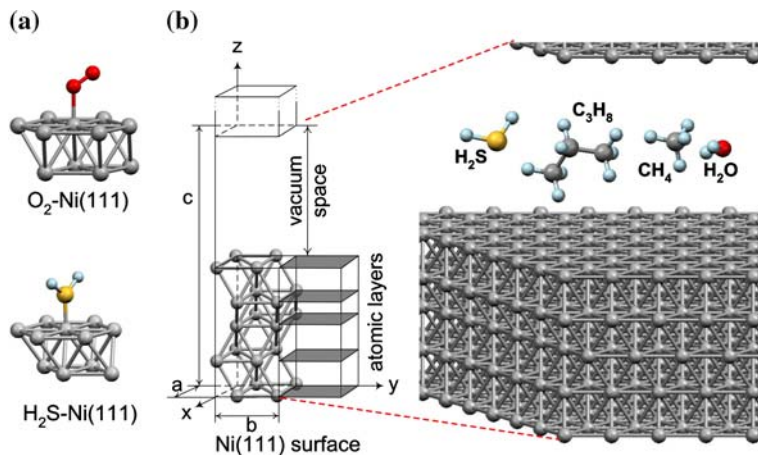


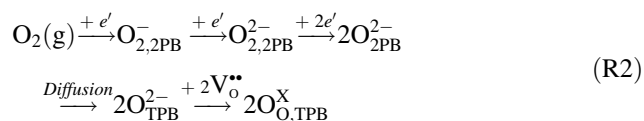
Neutral molecular oxygen first adsorbs on the surfaces, followed by charge transfer from the solid surface to the adsorbed oxygen species to form superoxo-like O₂⁻, peroxy-like O₂²⁻, or to dissociate to monatomic oxygen ions. The oxygen ions then have to move to the TPBs in order to combine with V_o^{••} in the electrolyte. Depending on the bulk and surface transport properties of cathode and electrolyte materials [13, 127], these elementary reactions may occur via several parallel routes. The first route (**R1**) is through the TPBs without the involvement of any surface transport. When a gaseous oxygen molecule is directly adsorbed, reduced, dissociated, and incorporated at the TPB, the reaction sequence can be described as follows,



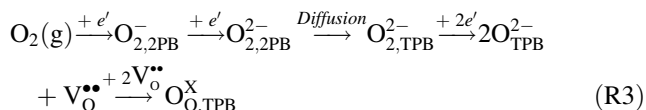
The second route (**R2**) is a process mediated by the diffusion of oxygen species along the electrode surface (a 2PB). A gaseous oxygen molecule is adsorbed (and/or reduced and dissociated to monatomic oxygen species) at a cathode surface (a 2PB), followed by diffusion of oxygen ions along the cathode surface to the TPB, where it is incorporated:

Fig. 3 Illustration of (a) the cluster model and (b) the slab model for computations of gas–solid interactions in SOFCs. Molecules in the vacuum space are not scaled





The third route (**R3**) is a process mediated by the diffusion of the adsorbed oxygen along the electrolyte surface (2PBs). A gaseous oxygen molecule adsorbs on the electrolyte surface (2PBs), followed by transport along the electrolyte surface to or near the TPB, where the oxygen species are reduced and incorporated into the electrolyte.



The last route is a process mediated by the diffusion or tunneling of electrons from the electrode along the surface of the electrolyte (2PBs) to the adsorbed oxygen on the electrolyte surface. A gaseous oxygen molecule adsorbs on the electrolyte surfaces (2PBs), followed by reduction of the oxygen species by electrons from the electrode moving along the electrolyte surfaces. In this case, the oxygen species may be reduced and incorporated on the electrolyte surface.

Clearly, TPBs play a vital role in SOFCs when a metallic electrode is used, as evidenced from experimental observations [128, 129] in which the performances of cells with Pt or Ag electrode increase with the TPB length. Clearly, the longer the TPB length, the greater the number of active sites for oxygen reduction. Further, TPBs can be broadened by enhancing the transport of oxygen species along the 2PBs (electrode and electrolyte surfaces) as well as the tunneling of electrons away from the TPB along the electrolyte surfaces. To enhance the kinetics of oxygen reduction, one can reduce the energy barrier to oxygen reduction at the TPB and to transport of electronic and oxygen species along the 2PBs.

The reaction barriers can be examined using DFT calculations. For the first two charge-transfer steps in the reaction sequence (see reaction (6)), the metal surface donates its *d* orbital electrons to the $\text{O}_2 \pi^*$ orbital, leading to the formation of O_2 -metal chemical bonds. The molecular adsorption process without significant reaction barriers produces superoxo-like O_2^- and peroxy-like O_2^{2-} species. While the *d*-band electrons completely fill the anti-bonding orbitals of O_2 , the O–O bond starts to break, forming the O^{2-} ion (dissociation) in the third step. As a consequence, the reduction barrier is the energetic difference between the adsorption energy in the first two steps and the dissociation barrier in the third step. These energetic properties in the oxygen reduction process are directly related to the *d* orbital of the metallic surface and the π^* orbital of

molecularly adsorbed oxygen species. This can be analyzed by the *d*-band model [130] which states that the reactivity at the surfaces of late transition metals corresponds to the energetic shape and position of the *d*-band state of the metallic surface. It is known that the *d*-band structures and centers of the metallic surfaces at 2PB regions are affected by the metal elements, surface morphology and electric field, whereas the *d*-band properties of the metallic surfaces at the TPBs with metal/metal-oxide (i.e., electrode/electrolyte) interfaces are influenced by the subsurface elements (metal oxide) and electric field [130, 131].

According to previous studies on Pt and Ag surfaces [131, 132], the *d*-band shifting perturbed by an external electric field causes a small energetic change (<0.1 eV per V/Å) and may affect both 2PB and TPB regions. Therefore, the energetic difference of the oxygen reduction barriers at 2PBs and TPBs may depend primarily on the *d*-band of the metallic surfaces disturbed by either surface morphology or subsurface elements. It is expected that these differences can be quantitatively examined by applying accurate and cost-effective DFT calculations to minimize the uncertainty regarding the fundamental reaction sequences for oxygen reduction. In this section, we briefly review our current understanding of oxygen reduction at 2PBs and TPBs in cells with metallic electrodes.

Oxygen reduction on Pt and Ag surfaces (2PB). Compared to the oxygen interactions with metal-oxide surfaces, theoretical studies on metallic surfaces (2PBs) have been more extensively reported as summarized in [101]. In order to examine the oxygen reduction reaction at the 2PBs in SOFC applications, Pt [133–147] and Ag [116, 148–158] cathode materials will be discussed. It is well known that different surface morphologies, subsurface elements and surface charges induce *d*-band shifting of the metal electrodes and change O_2 dissociation barriers in different surface orientations [130]. For the surfaces of a pure metal, surface orientation can cause the large differences in energetics. Therefore, the variation of reduction barriers at 2PBs can be determined. For example, on Ag surfaces, dissociation barriers are 0.85–1.06 eV and 0.60–0.70 eV in Ag (111) [116, 158] and (110) [116, 149, 150] surface orientations, respectively, while those are 0.70–1.00 eV and 0.70–0.90 eV in Pt (111) [135, 136, 141, 146] and (211) [141, 146] surfaces, respectively. Based on these calculations, it can be summarized that the reduction barriers at metal electrodes (2PBs) are higher than 0.60 eV and the barrier changes induced by the surface morphology are less than 0.15 eV.

Oxygen reduction at metal/metal-oxide interfaces (TPBs). It is known that the metal-oxide electrolytes (i.e., YSZ and GDC) can change the chemical properties of the surface metal layers (electrodes), and influence the oxygen reduction reaction at TPBs. A recent study on

$O_2/Ag-CeO_2$ reactions [116] demonstrated that the O_2 dissociation barriers reduced to 0.28–0.43 eV on the modeled TPBs of an Ag-monolayer-covered $CeO_2(111)$ surface as schematically displayed in Figs. 4 and 5. The values in brackets represent Bader charges [159–162] of the adsorbed oxygen species.

Compared with the reaction on pure Ag surfaces (2PBs), the dissociation barriers at TPBs remarkably decreased about 0.17–0.57 eV because the subsurface O layer of $CeO_2(111)$ upshifts the d -band center of the surface Ag layer, making them more reactive. The effects were also demonstrated with DFT calculations of Ag(111) with subsurface O layers [152, 158]. Enhanced catalytic ability from the subsurface interaction was also studied for other metal/metal oxide systems [163–166]. According to the reduction barrier calculations, the decreasing of the O_2 dissociation barrier induced from surface morphology is smaller than that from subsurface elements, implying that the oxygen reduction reaction is more kinetically favorable to occur at TPBs than at 2PBs as discussed in the previous section.

When oxygen is reduced at TPBs, the reduced O^{2-} ions can be directly incorporated into the bulk of the electrolyte without a well-defined transition state as shown in the $O_2/Ag/CeO_2$ system [116]. In contrast, when oxygen is reduced at the electrode surface (2PBs), the reduced O^{2-} ions have to diffuse along the surfaces of the metallic electrode to TPBs in order to combine with $V_O^{\bullet\bullet}$. If the diffusion barriers of O^{2-} ions from 2PBs to TPBs are significant, it reduces the chance for the cathode reaction via **R2** and **R3**. To verify the assumption, the most widely used metallic electrodes (Pt and Ag) were examined. Two pathways may be possible for O^{2-} ion diffusion from 2PBs to 3PBs—diffusion through the bulk or on the surface. Because the metallic electrodes are not ionic conductors, the O^{2-} ions are much less likely to diffuse inside the bulk. Experimentally, it is known that oxygen species can diffuse

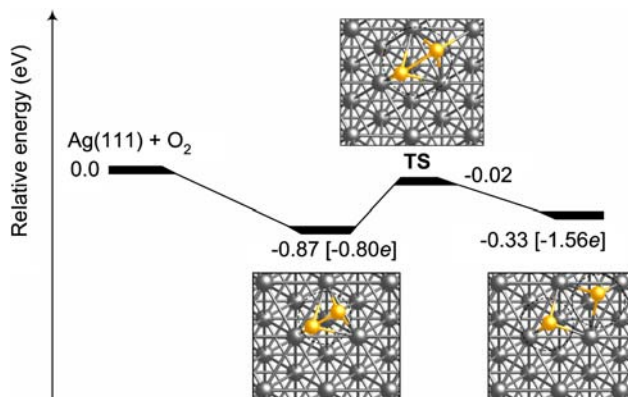


Fig. 4 A potential energy profile of the oxygen reduction reaction on Ag(111)

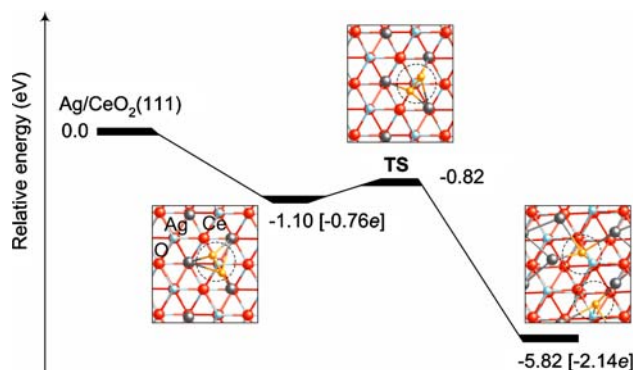


Fig. 5 A potential energy diagram of the oxygen reduction reaction at the interface of Ag- CeO_2

through the Ag bulk in (110) direction, but this process requires high O_2 concentrations and high temperatures (600–900 K) [167–170]. Computational studies also demonstrated that even the first layer diffusion process for the O/Ag system needs to overcome a high reaction barrier (>0.86 eV) [152, 156], whereas the migration barriers on Pt and Ag surfaces are relatively low. The barriers from fcc to hcp sites on Pt(111) surfaces are varied from 0.43 eV to 0.58 eV [134, 171–173], whereas that on the Ag(111) surfaces is 0.37 eV. The migration barriers in (1 $\bar{1}$ 0) and (001) directions on Ag(110) are 0.17 and 0.43 eV, respectively [116].

In summary, TPBs play a vital role in the functioning of a metallic cathode for SOFCs. The catalytic properties of the TPBs are determined by the nature of both the metallic electrode and the electrolyte. The catalytically active TPB lines may be broadened somewhat by the surface transport of oxygen species and electrons along the electrode and electrolyte surfaces (2PBs). Quantum-chemical calculations may provide useful insight to better design of catalytically active TPBs or effective approaches to broadening the TPB lines into TPB zones for oxygen reduction. In general, it is anticipated that the area-specific-resistance (ASR) of a metal-based cathode decreases with the TPB length per unit area until the broadened TPB zones overlap.

3.2.2 Oxygen Reduction on $LaMnO_3$ -Based Cathode Materials

Some of the bulk properties of $LaMnO_3$ -based materials have been determined using several experimental methods, including X-ray powder diffraction [174] and Raman spectroscopy [175, 176]. The electronic structure of $LaMnO_3$ has been theoretically predicted using first-principles calculations [177–180]. In particular, a number of interesting studies of the surfaces of SOFC cathode

materials have been reported, including atomistic modeling [181] and ab initio calculations [182] for $\text{LaMnO}_3(110)$, atomic and electronic structure calculations for $\text{LaMnO}_3(001)$ [183], HF calculations of $\text{LaMnO}_3(001)$ and (110) [184], DFT calculations for LaMnO_3 and SrMnO_3 [185], and thermodynamic stability of LaMnO_3 [186]. In addition to ab initio methods, semi-empirical methods have also been applied, including a force field method [187] and molecular dynamics (MD) [188, 189]. Shown in Fig. 6a is the ideal cubic LaMnO_3 structure with space group $Pm\bar{3}m$. Due to the Jahn-Teller (JT) effect of the $3d^4 \text{Mn}^{3+}$ ions, the cubic structure can be distorted to orthorhombic structure ($Pnma$) at low temperatures [177, 190] (see Fig. 6b). However, as Evarestov and coworkers [182] reported, the JT effect does not influence lattice deformation under the conditions for typical SOFC operation. Thus, we considered only the highly symmetric cubic perovskite structure of $Pm\bar{3}m$ for surface calculations of O_2 - LaMnO_3 interactions in SOFCs. Fig. 6c shows an example of the 2D slab model for $\text{LaMnO}_3(110)$. Kotomin and coworkers explored the possible importance of the MnO_2 -terminated $\text{LaMnO}_3(001)$ surface, reporting surface calculations and a higher surface stability than that of O-terminated $\text{LaMnO}_3(110)$ [183].

Based on the previous studies, we have recently examined oxygen reduction at LaMnO_3 -based cathode materials using periodic slab model calculations as implemented in the VASP code [113, 114]. All calculations were carried out with the projector augmented wave (PAW) [191] method. We applied the GGA with the Perdew-Wang (PW91) functional [104]. A 400 cut-off energy and $(4 \times 4 \times 4)$ Monkhorst-Pack mesh [192] k-points were used. In terms of the surface stability, we found that the (110) surface is slightly less stable than (100) using the

spin-polarization method (1.37 and 0.83 J/m^2 , respectively) [117] (see Fig. 7a, b), which is in agreement with the previous work [183]. However, in order to examine the effects of La and Mn cations including doping elements such as Sr^{2+} , we chose the LaMnO - and O-terminated $\text{LaMnO}_3(110)$ surfaces for O_2 interactions. As shown in Fig. 7, LaMnO_3 - and O-terminated surface models—perfect configurations—containing a total of 20 ions (four La, four Mn, and 12 O ions) were initially applied. We found that the O-terminated surface is energetically less stable than the LaMnO -terminated surface according to the comparison of predicted adsorption energies estimated using the spin-polarization method (-0.04 eV and $-7.38 < \Delta E_{\text{ads}} < -1.51 \text{ eV}$, respectively). Molecularly adsorbed intermediates are superoxo- or peroxy-like species—their predicted O–O vibrational frequencies range from 957 cm^{-1} to $1,207 \text{ cm}^{-1}$, respectively. This prediction may help the interpretation of experimental measurements such as vibrational spectra [193]. In particular, similar to the calculations on LaMnO_3 surfaces, and as illustrated in Fig. 8, we carried out DFT calculations to locate plausible intermediates and products of O_2 on LaMn -terminated $\text{La}_{0.5}\text{Sr}_{0.5}\text{MnO}_3(110)$ [194]. To construct a surface model representing $\text{La}_{0.5}\text{Sr}_{0.5}\text{MnO}_3$ (LSM0.5), the LaMnO -terminated (110) surface (Fig. 7c) was used by replacing the La^{3+} ions with Sr^{2+} ions, accompanied by the formation of doubly charged oxygen vacancies. The Bader charge analysis [159–162] clearly suggests that charge was transferred from the substrate to the adsorbed oxygen species. In addition, ab initio MD calculations (using the VASP code) for the interactions between O_2 and $\text{La}_{0.5}\text{Sr}_{0.5}\text{MnO}_3(110)$ at 1,073 K were performed to simulate SOFC operating conditions. To construct non-bonded O_2 and a clean LSM0.5, the distance between an O_2

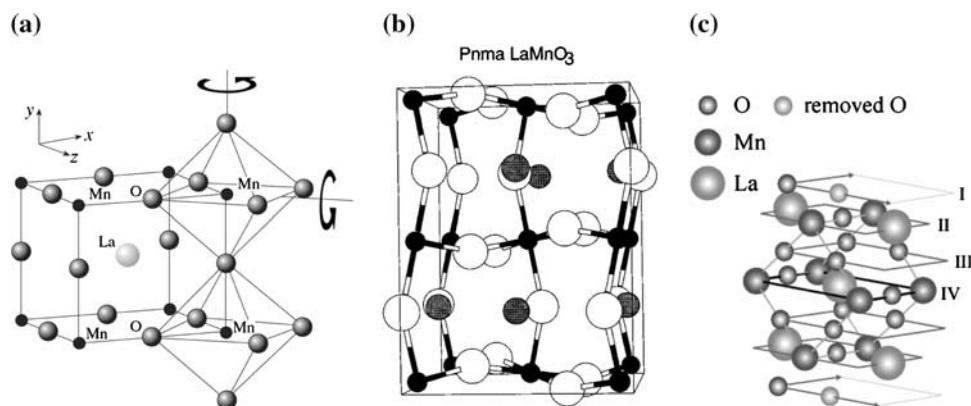
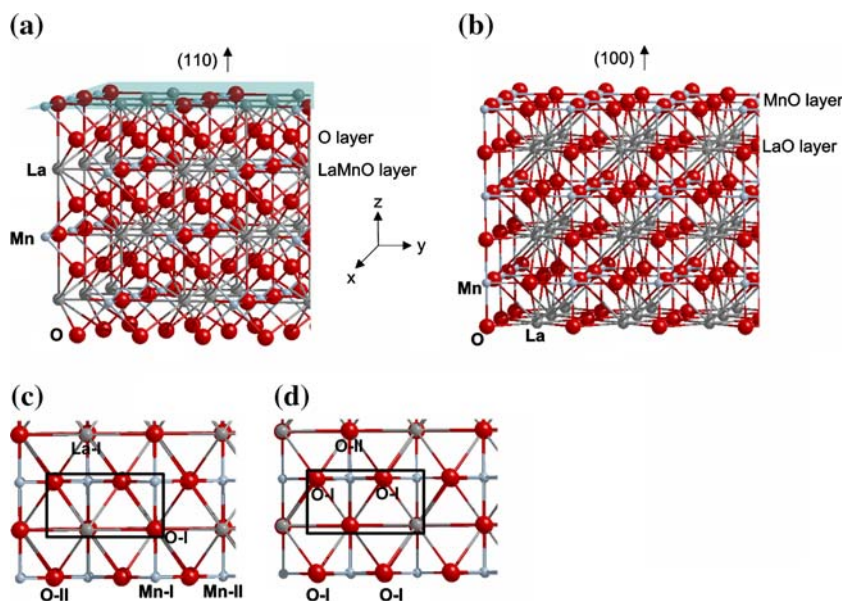


Fig. 6 (a) The crystal structure of cubic ($Pm\bar{3}m$) LaMnO_3 [190]. With kind permission of Springer Science and Business Media. (b) The crystal structure of orthorhombic ($Pnma$) LaMnO_3 . La, Mn, and O are in gray, small black, and white, respectively [177]. Reprinted figure with permission from W. E. Pickett and D. J. Singh, *Physical Review B*, Vol. 53, 1146–1160, 1996. Copyright© 1996 by the

American Physical Society. (c) A typical surface model of $\text{LaMnO}_3(110)$ [182]. This article was published in *Solid State Communications*, Vol. 127, R. A. Evarestov, E. A. Kotomin, E. Heifets, J. Maier and G. Borstel, *Ab initio* Hartree-Fock calculations of $\text{LaMnO}_3(110)$ surfaces, Page 367–371, Copyright Elsevier © 2003

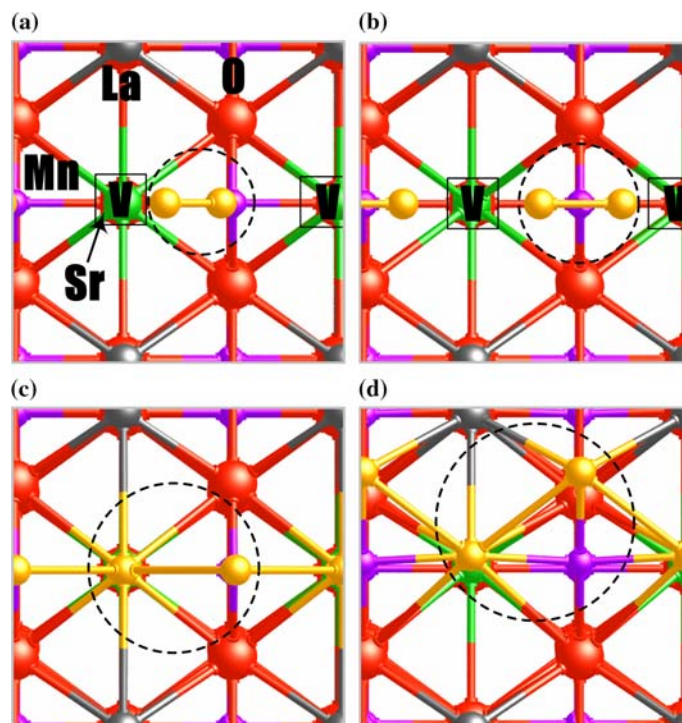
Fig. 7 Surface models of the slab model calculations for the surface stability and O₂-LaMnO₃ interactions. Side views of (a) (110) and (b) (100) surfaces. Top views of (c) LaMnO- and (d) O-terminated surfaces of LaMnO₃(110). **I** and **II** are the atoms on the top and second layers, respectively. The rectangles denote the supercells [117]. Reprinted with permission from Chemistry of Materials, Vol. 19, 1690–1699, 2007. Copyright © 2007 American Chemical Society



molecule and the LSM0.5 was initially set at ~ 4.8 Å. A time step of 2 fs and the Nosé-Hoover thermostat [195] were applied for the MD simulations. As oxygen molecule adsorbs at the Mn ion, the energy decreases after an initial energy fluctuation. Shown in Fig. 9 are snapshots of important states and energy variations as a function of time. Due to the rotation of O₂ in the course of the initial process, a hill at ~ 80 fs is produced. In ~ 130 fs, a superoxo-like species with an exothermicity of ~ 2.0 eV (compared to La_{0.5}Sr_{0.5}MnO₃ + O₂) was produced. After

converting to a peroxo-like species in ~ 430 fs, one of the oxygen atoms of the peroxo-like configuration incorporates into the oxygen vacancy without barrier at ~ 530 fs. The oxygen species adsorbed on Mn diffuses to a more stable site at ~ 570 fs. The whole process is completed with a highly exothermic energy of ~ 8.5 eV. According to the calculations using the LaMnO₃ and La_{0.5}Sr_{0.5}MnO₃ surfaces models, we found oxygen vacancies enhance O₂ dissociation kinetics—energetically more favorable on a defective surface than a perfect surface—and the whole

Fig. 8 Geometrical illustration for O₂ interactions on La_{0.5}Sr_{0.5}MnO₃(110): (a) superoxo-like species on Mn, (b) peroxo-like species on Mn, (c) after dissociation/incorporation into the bulk phase, and (d) diffusion to a more stable site on the surface. **V** denotes a doubly charged oxygen vacancy



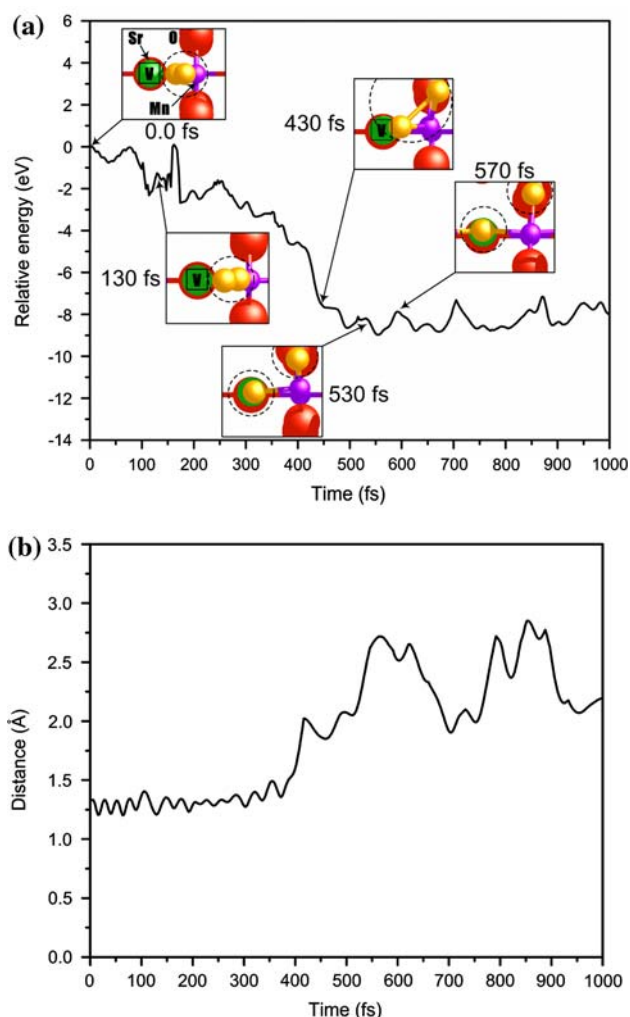
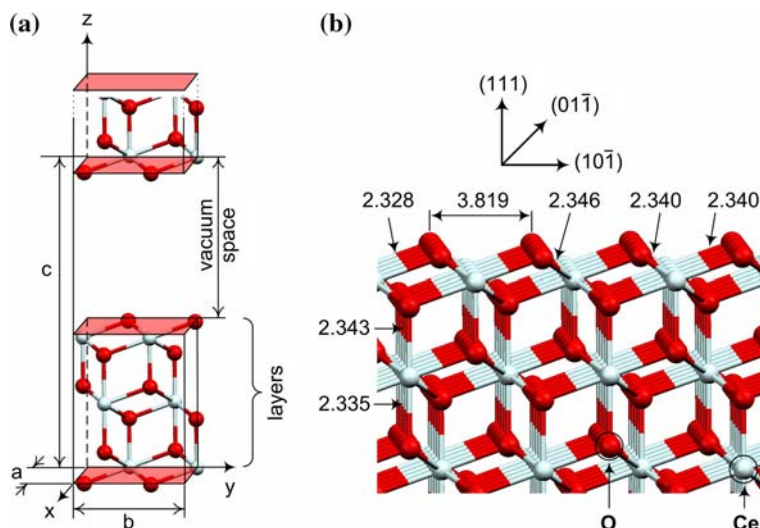


Fig. 9 MD simulations for dissociative molecular adsorption on $\text{La}_{0.5}\text{Sr}_{0.5}\text{MnO}_3$ at 1073 K. \mathbf{V} denotes a doubly charged oxygen vacancy

Fig. 10 (a) A 2D slab model for O_2 interactions with CeO_2 . (b) An estimated bulk structure of CeO_2 . Bond lengths are in the unit of Å [115]. Reproduced with permission from ChemPhysChem from Wiley-VCH, 2006, Vol. 7, 1957–1963



reduction reaction may occur without well-defined reaction barriers. Based on the mechanistic studies, it is possible to predict oxygen surface exchange coefficients for LSM0.5 measured by SIMS [42, 43].

3.2.3 Oxygen Interaction with an Electrolyte

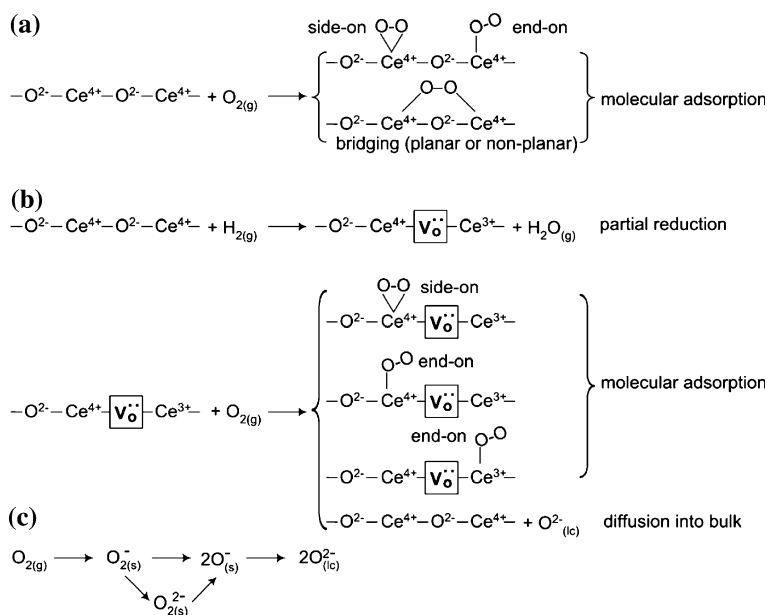
In this section, we will discuss a recent theoretical study [115] coupled with in situ Raman spectroscopy to examine oxygen interactions with CeO_2 (2PBs). In situ Raman spectroscopy is a powerful tool to probe vibrational excitation and lattice transformation [196] as well as the molecular details of O_2 - CeO_2 interactions under SOFC operating conditions. In particular, the application of Raman spectroscopy to patterned electrodes [197] may provide more detailed information on active reaction sites of cathode materials. In a study of the interaction between O_2 and $\text{La}_{0.6}\text{Sr}_{0.4}\text{MnO}_3$ using Raman spectroscopy [193], an oxygen peak was observed at room temperature and 403 K on the $\text{La}_{0.6}\text{Sr}_{0.4}\text{MnO}_3$ surface with and without Ag modification, leading to the shift of Raman peak from 820 cm^{-1} to 802 cm^{-1} , respectively. Choi and coworkers [115] pointed out the significance of establishing a computational framework to elucidate oxygen reduction at the cathode materials by employing in situ Raman micro-spectroscopy and quantum-chemical calculations. In the study, CeO_2 was used as a benchmark system because it has been widely used as an SOFC electrolyte by doping with rare-earth elements (i.e., gadolinia-doped ceria or GDC) for lower temperature SOFCs [198–200]. Periodic slab model calculations (see Fig. 10) coupled with in situ Raman micro-spectroscopy were successfully applied to interpret the Raman peaks corresponding to the adsorbed

oxygen species on CeO₂ surfaces, which were verified by isotope-substitution experiments. The theory predicted geometrical information, energetics, and vibrational frequencies after locating various oxygen species at active sites on both unreduced and partially reduced CeO₂ surfaces. By comparing the measured oxygen bands at 825 and 1,131 cm⁻¹ (peroxo- and superoxo-like species, respectively) with DFT results, it was found that the oxygen-vacancy location affects the formation and dissociation of adsorbed oxygen species. It was also reported that reduced CeO₂ is energetically more favorable than unreduced surface CeO₂, similar to the O₂-LaMnO₃ interactions described in the previous section. Shown in Fig. 11 are the reaction sequence and mechanism for oxygen reduction on the CeO₂ surfaces. Similar computational framework may be applied to examine O₂ interactions with other materials.

4 Perspectives for the Application of Quantum-Chemical Calculations to Design of SOFC Materials

Quantum-chemical calculations may provide us with insight vital to achieving intelligent design of novel materials with unusual transport and catalytic properties for a new generation of SOFCs [73]. Because of the vast number of possibilities (candidate materials and structures), the complexity of the interfacial phenomena associated with each, and the intensive efforts required for computations, however, an efficient strategy must be employed to rationally reduce the number of enormous possibilities for design of novel materials using first-principles based calculations. In this section, we briefly review two theoretical approaches.

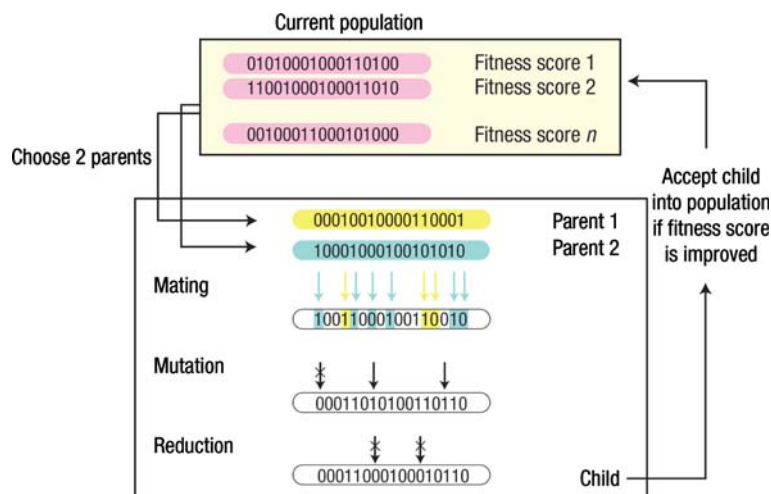
Fig. 11 Adsorption of oxygen species on (a) an unreduced and (b) partially reduced CeO₂ surfaces. (c) A stepwise reaction sequence of the oxygen reduction reaction, where (g), (s), (lc), and V_O^{••} denote gas, surface, lattice, and an oxygen vacancy, respectively [115]. Reproduced with permission from ChemPhysChem from Wiley-VCH, 2006, Vol. 7, 1957–1963



Application of Genetic-Algorithm based Techniques. First-principles approaches can be coupled with statistical approaches (e.g., expert system, simulated annealing, and neural network) [201] to screen possible SOFC cathode materials. Here we introduce a promising statistical tool—a genetic algorithm developed by Holland [202]—to accelerate the design of novel cathode materials using quantum-chemical calculations. Genetic-algorithm based approaches have been widely applied in materials design and processing [203], including the optimization of Si [204] and Cu clusters [205], tight-binding parameter calculations for Si [206], the determination of the ground-state geometry of C₆₀ [207], the identification of ground-state structures of Ta-W and TiN with vacancies [208], and the prediction of the most stable alloys composed of four elements [209]. Genetic algorithms are highly efficient optimization approaches based on Darwin’s evolutionary theory and natural selection [201, 203]. The genetic algorithms require three key processes [203, 208]; mating (or crossover) of parents for a genetic exchange, mutation for a genetic makeup, and reduction (or selection) for a new generation among parents, mutants, and children, as schematically illustrated in Fig. 12. The process undergoes until it reaches a steady state.

Jóhannesson and coworkers [209] recently reported an exhaustive study using a genetic algorithm in conjunction with periodic DFT calculations to screen the most stable 20 alloys comprising four elements. The screening was performed using 32 elements in fcc and bcc configurations with 192016 possibilities, providing a good agreement with the available experimental data. The technique coupling quantum-chemical calculations with a genetic algorithm is very promising for the application as a screening tool to

Fig. 12 Schematic of a genetic algorithm for obtaining a model hamiltonian [208]. Reprinted by permission from Macmillan Publishers Ltd: Nature Materials, Vol. 4, 391–394, 2005, copyright © 2005



search initial plausible ground-state geometries for high efficient cathode materials, especially for perovskite ABO₃ cathodes.

Application of Theoretical Combinatorial Materials Science. Experimental combinatorial materials science [210, 211] has become popular in developing new materials with desired properties, including screening of electrochemical catalysts [212] and electrochemical testing systems [213]. Strasser and coworkers [81] reported an experimental and theoretical study of screening novel fuel cell anode materials by means of a combinatorial methodology. An anode array comprised of 64 elements based on Pt, Ru, CO, Ni, and W were evaluated in terms of CO tolerance, and PtRuCo alloys showed the best performance. In particular, theoretical screening tests were carried out by using periodic DFT methods with surface models as shown in Fig. 13. Summarized in Fig. 13b are the predicted surface activities on ternary MPt₂/Ru alloys according to $-1/2\Delta E_{\text{H}_2} + \Delta E_{\text{CO}}$, where ΔE_{H_2} and ΔE_{CO} represent the adsorption energies of H₂ and CO. The calculations predict that PtRuCo has better performance than PtRu and PtRuNi, which is in line with the experimental results. Similar to the computational framework in parallel with experimental measurements, ABO₃ cathode materials for SOFCs can be screened with in situ potential-dependent vibrational

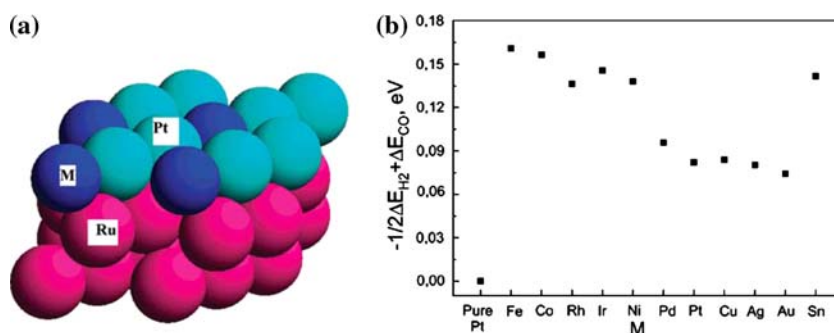
spectroscopy performed on cells with a patterned electrode of precisely controlled geometry [197].

5 Concluding Remarks

While the oxygen reduction processes at an SOFC cathode have been extensively studied both experimentally and theoretically, many fundamental questions regarding the processes still remain unanswered, especially for perovskite-type cathode materials. To achieve intelligent design of new cathode materials, the detailed molecular processes relevant to oxygen reduction must be theoretically predicted using first-principles based computations and experimentally probed or mapped using in situ characterization techniques such as vibrational spectroscopy. Further, multi-scale modeling techniques are needed to link these microscopic properties to the electrochemical performance (current-voltage characteristics and impedance spectra) of a component or a cell, which can be directly measured using electrochemical techniques.

Since TPBs represent one of the most important active sites for electrochemical reactions in SOFCs [214], understanding the oxygen reduction processes at or near TPBs is vital to the understanding of the detailed reaction

Fig. 13 (a) Illustration of a surface model for modified Ru(0001), MPt₂/Ru, where M denotes Fe, Co, Rh, Ir, Ni, Pd, Pt, Cu, Ag, Au, or Sn [81]. (b) Calculated surface activities on ternary alloys, MPt₂/Ru [81]. Reprinted with permission from Journal of Physical Chemistry B, Vol. 107 (40), 11013–11021, 2003. Copyright © 2003 American Chemical Society



mechanisms in SOFCs. However, one of the key challenges is the construction of proper surface/interface models for the junctures between electrolyte and electrode (i.e., the YSZ-LSM interface). Both phase mismatch [215, 216] between different materials and their most stable surface orientations must be taken into consideration to construct reliable interfacial surface models. Further, because quantum-chemical calculations are traditionally performed at 0 K in vacuum, development of ab initio thermodynamics (or proper thermodynamic corrections) [217] is imperative to properly simulate SOFC operating conditions. Finally, catalytic properties of SOFC cathode materials toward oxygen reduction can also be explored by establishing kinetic parameters using kinetic theories [218, 219].

Acknowledgements This work was supported by DOE-NETL University Coal Program (Grant No. DE-FG26-06NT42735) and DOE Basic Energy Science (Grant No. DE-FG02-06ER15837) and was partly performed using the MSCF in EMSL at Pacific Northwest National Laboratory (PNNL), a national scientific user facility sponsored by the U.S. DOE and OBER.

References

- Dresselhaus MS, Thomas IL (2001) *Nature* (London, United Kingdom) 414:332
- Steele BCH, Heinzel A (2001) *Nature* (London, United Kingdom) 414:345
- Minh NQ, Takahashi T (1995) *Science and technology of ceramic fuel cells*. Elsevier Science, Amsterdam
- Singhal SC, Kendall K (2003) *High-temperature solid oxide fuel cells: fundamentals, design and applications*. Elsevier Science
- Minh NQ (2004) *Solid State Ionics* 174:271
- Singhal SC (2002) *Solid State Ionics* 152:405
- Minh NQ (1993) *J Am Ceram Soc* 76:563
- Singh P, Minh NQ (2004) *Int J Appl Ceram Technol* 1:5
- Yamanoto O (2000) *Electrochim Acta* 45:2423
- <http://www.netl.doe.gov/seca/>
- Xia C, Liu M (2002) *Adv Mater* 14:521
- Zuo C, Zha S, Hatano M, Uchiyama M, Liu M (2006) *Adv Mater* 18:3318
- Adler SB (2004) *Chem Rev* 104:4741
- Mebane DS, Liu M (2006) *J Solid State Electrochem* 10:575
- Pizzini S (1973) In: Gool Wv (ed) *Fast ion transport in solids*. North-Holland, p 461
- Liu M, Winnick J (1999) *Solid State Ionics* 118:11
- Endo A, Ihara M, Komiyama H, Yamada K (1996) *Solid State Ionics* 86:1191
- Endo A, Fukunaga H, Wen C, Yamada K (2000) *Solid State Ionics* 135:353
- Ioroi T, Hara T, Uchimoto Y, Ogumi Z, Takehara Z (1997) *J Electrochem Soc* 144:1362
- Mizusaki J, Saito T, Tagawa H (1996) *J Electrochem Soc* 143:3065
- Takeda Y, Kanno R, Noda M, Tomida Y, Yamamoto O (1987) *J Electrochem Soc* 134:2656
- Endo A, Wada S, Wen CJ, Komiyama H, Yamada K (1998) *J Electrochem Soc* 145:L35
- Sasaki K, Wurth JP, Gschwend R, Godickemeier M, Gauckler LJ (1996) *J Electrochem Soc* 143:530
- Adler SB (1998) *Solid State Ionics* 111:125
- Baumann FS, Fleig J, Habermeier HU, Maier J (2006) *Solid State Ionics* 177:1071
- Lauret H, Hammou A (1996) *J Eur Ceram Soc* 16:447
- Siebert E, Hammouche A, Kleitz M (1995) *Electrochim Acta* 40:1741
- Kuznecov M, Otschik P, Trofimenko N, Eichler K (2004) *Russ J Electrochem* 40:1162
- Jiang SP, Love JG (2001) *Solid State Ionics* 138:183
- Jiang SP, Love JG (2003) *Solid State Ionics* 158:45
- Kuo JH, Anderson HU, Sparlin DM (1989) *J Solid State Chem* 83:52
- Mizusaki J, Mima Y, Yamauchi S, Fueki K, Tagawa H (1989) *J Solid State Chem* 80:102
- Mizusaki J, Mori N, Takai H, Yonemura Y, Minamiue H, Tagawa H, Dokiya M, Inaba H, Naraya K, Sasamoto T, Hashimoto T (2000) *Solid State Ionics* 129:163
- Poulsen FW (2000) *Solid State Ionics* 129:145
- Nowotny J, Rekas M (1998) *J Am Ceram Soc* 81:67
- van Hassel BA, Kawada T, Sakai N, Yokokawa H, Dokiya M, Bouwmeester HJM (1993) *Solid State Ionics* 66:295
- Mizusaki J, Yonemura Y, Kamata H, Ohyama K, Mori N, Takai H, Tagawa H, Dokiya M, Naraya K, Sasamoto T, Inaba H, Hashimoto T (2000) *Solid State Ionics* 132:167
- Kamata H, Yonemura Y, Mizusaki J, Tagawa H, Naraya K, Sasamoto T (1995) *J Phys Chem Solids* 56:943
- Kawada T, Masuda K, Suzuki J, Kaimai A, Kawamura K, Nigara Y, Mizusaki J, Yugami H, Arashi H, Sakai N, Yokokawa H (1999) *Solid State Ionics* 121:271
- Horita T, Yamaji K, Ishikawa M, Sakai N, Yokokawa H, Kawada T, Kato T (1998) *J Electrochem Soc* 145:3196
- Bouwmeester HJM, Den Otter MW, Boukamp BA (2004) *J Solid State Electrochem* 8:599
- De Souza RA, Kilner JA (1998) *Solid State Ionics* 106:175
- De Souza RA, Kilner JA (1999) *Solid State Ionics* 126:153
- De Souza RA, Kilner JA, Walker JF (2000) *Mater Lett* 43:43
- Huang KQ, Goodenough JB (2001) *J Electrochem Soc* 148:E203
- Kilner JA, DeSouza RA, Fullarton IC (1996) *Solid State Ionics* 86:703
- Lane JA, Benson SJ, Waller D, Kilner JA (1999) *Solid State Ionics* 121:201
- Lane JA, Kilner JA (2000) *Solid State Ionics* 136:997
- Zipprich W, Waschilewski S, Rocholl F, Wiemhofer HD (1997) *Solid State Ionics* 101:1015
- Zipprich W, Wiemhofer HD (2000) *Solid State Ionics* 135:699
- Brumleve TR, Buck RP (1978) *J Electroanal Chem* 90:1
- Brumleve TR, Buck RP (1981) *J Electroanal Chem* 126:73
- Bisquert J, Gratzel M, Wang Q, Fabregat-Santiago F (2006) *J Phys Chem B* 110:11284
- Jamnik J, Maier J (2001) *Phys Chem Chem Phys* 3:1668
- Coffey GW, Pederson LR, Rieke PC (2003) *J Electrochem Soc* 150:A1139
- Adler SB, Lane JA, Steele BCH (1996) *J Electrochem Soc* 143:3554
- Deseure J, Bultel Y, Dessemond L, Siebert E (2005) *Electrochim Acta* 50:2037
- Svensson AM, Sunde S, Nisancioglu K (1997) *J Electrochem Soc* 144:2719
- Svensson AM, Sunde S, Nisancioglu K (1998) *J Electrochem Soc* 145:1390
- Williford RE, Singh P (2004) *J Power Sources* 128:45
- Newman J, Thomas-Alyea KE (2004) *Electrochemical systems*. Wiley-Interscience, Hoboken
- Fleig J (2002) *J Power Sources* 105:228
- Fleig J, Pham P, Sztulzaft P, Maier J (1998) *Solid State Ionics* 115:739

64. Herbstritt D, Weber A, Ivers-Tiffée E (2001) *J Eur Ceram Soc* 21:1813
65. Fleig J, Maier J (2004) *J Eur Ceram Soc* 24:1343
66. Koep E, Mebane DS, Das R, Compson C, Liu M (2005) *Electrochem Solid State Lett* 8:A592
67. Brichzin V, Fleig J, Habermeier HU, Cristiani G, Maier J (2002) *Solid State Ionics* 152:499
68. Mebane DS, Liu Y, Liu M (2007) *J Electrochem Soc* 154:A421
69. Liu M, Lu X, Faguy P (2003) Proceedings of solid oxide fuel cells VIII
70. Lu X, Faguy PW, Liu M (2003) Proceedings of solid-state ionic devices III
71. Lu X, Faguy PW, Liu M (2002) *J Electrochem Soc* 149:A1293
72. Bockris JOM, Khan SUM (1993) *Surface electrochemistry*. Plenum, New York
73. Broadbelt LJ, Snurr RQ (2000) *Appl Catal A* 200:23
74. Ruetz F (ed) (1992) *Quantum chemistry approaches to Chemisorption and Heterogeneous catalysis*. Kluwer Academic Publisher, Boston
75. Santen RA (1991) *Theoretical Heterogeneous catalysis*. World Scientific, Singapore
76. Hermse CGM, van Bavel AP, Koper MTM, Lekkien JJ, van Santen RA, Jansen APJ (2004) *Surf Sci* 572:247
77. Jacobsen CJH, Dahl S, Clausen BS, Bahn S, Logadottir A, Nørskov JK (2001) *J Am Chem Soc* 123:8404
78. Linic S, Barteau MA (2004) *J Am Chem Soc* 126:8086
79. Linic S, Jankowiak J, Barteau MA (2004) *J Catal* 224:489
80. Neurock M (2003) *J Catal* 216:73
81. Strasser P, Fan Q, Devenney M, Weinberg WH, Liu P, Nørskov JK (2003) *J Phys Chem B* 107:11013
82. Gokhale AA, Kandoi S, Greeley JP, Mavrikakis M, Dumesic JA (2004) *Chem Eng Sci* 59:4679
83. Levine IN (1991) *Quantum chemistry*. Prentice-Hall Inc., NJ
84. Lowe JP (1993) *Quantum chemistry*. Academic Press
85. Atkins PW (1983) *Molecular quantum mechanics*. Oxford University Press
86. Harrison WA (1989) *Electronic structure and the properties of solids: the physics of the chemical bond*. Dover Publications, Inc., NY
87. Szabo A, Ostlund NS (1982) *Modern quantum chemistry: introduction to advanced electronic structure theory*. MacMillan, NY
88. Jensen F (1999) *Introduction to computational chemistry*. John Wiley & Sons, Inc., New York
89. Hehre WJ, Radom L, Schleyer PvR, Pople JA (1986) *Ab initio molecular orbital theory*. John Wiley & Sons, Inc., New York
90. Born M, Oppenheimer JR (1927) *Ann Physik* 84:457
91. Greeley J, Nørskov JK, Mavrikakis M (2002) *Annu Rev Phys Chem* 53:319
92. From the beginning in Latin
93. Pople JA, Santry DP, Segal GA (1965) *J Chem Phys* 43:S129
94. Pople JA, Nesbet RK (1954) *J Chem Phys* 22:571
95. Roothaan CJC (1960) *Rev Mod Phys* 32:179
96. Binkley JS, Pople JA, Dobosh PA (1974) *Mol Phys* 28:1423
97. Møller C, Plesset MS (1934) *Phys Rev* 46:618
98. Bartlett RJ (1989) *J Phys Chem* 93:1697
99. Roos BO (1987) *Adv Chem Phys* 69:399
100. Kohn W, Sham LJ (1965) *Phys Rev* 140:1133
101. Shi Z, Zhang JJ, Liu ZS, Wang HJ, Wilkinson DP (2006) *Electrochimica Acta* 51:1905
102. Hohenberg P, Kohn W (1964) *Phys Rev B* 136:B864
103. Perdew JP, Chevary JA, Vosko SH, Jackson KA, Pederson MR, Singh DJ, Fiolhais C (1992) *Phys Rev B* 46:6671
104. Perdew JP, Wang Y (1992) *Phys Rev B* 45:13244
105. Perdew JP, Burke K, Ernzerhof M (1996) *Phys Rev Lett* 77:3865
106. Jacob T, Goddard WA III (2006) *ChemPhysChem* 7:992
107. Choi YM, Compson C, Lin MC, Liu M (2007) *J Alloys Comp* 427:25
108. Choi YM, Compson C, Lin MC, Liu M (2006) *Chem Phys Lett* 421:179
109. Frisch MJ, Trucks GW, Schlegel HB, Scuseria GE, Robb MA, Cheeseman JR, Montgomery JJA, Vreven T, Kudin KN, Burant JC, Millam JM, Iyengar SS, Tomasi J, Barone V, Mennucci B, Cossi M, Scalmani G, Rega N, Petersson GA, Nakatsuji H, Hada M, Ehara M, Toyota K, Fukuda R, Hasegawa J, Ishida M, Nakajima T, Kitao YH, Nakai H, Klene M, Li X, Knox JE, Hratchian HP, Cross JB, Adamo C, Jaramillo J, Gomperts R, Stratmann RE, Yazyev O, Austin AJ, Cammi R, Pomelli C, Ochterski JW, Ayala PY, Morokuma K, Voth GA, Salvador P, Dannenberg JJ, Zakrzewski VG, Dapprich S, Daniels AD, Strain MC, Farkas O, Malick DK, Rabuck AD, Raghavachari K, Foresman JB, Ortiz JV, Cui Q, Baboul AG, Clifford S, Cioslowski J, Stefanov BB, Liu G, Liashenko A, Piskorz P, Komaromi I, Martin RL, Fox DJ, Keith T, Al-Laham MA, Peng CY, Nanayakkara A, Challacombe M, Gill PMW, Johnson B, Chen W, Wong MW, Gonzalez C, Pople JA (2004) *Gaussian 03, Revision C.01*. Gaussian, Inc., Wallingford CT
110. Werner H-J, Knowles PJ, Schütz M, Lindh R, Celani P, Korona T, Pritchard G, Manby FR, Amos RD, Bernhardsson A, Berning A, Cooper DL, Deegan MJO, Dobbyn AJ, Eckert F, Hampel C, Hetzer G, Lloyd AW, McNicholas SJ, Meyer W, Mura ME, Nicklaß A, Palmieri P, Pitzer R, Schumann U, Stoll H, Stone AJ, Tarroni R, Thorsteinsson T (2006) *MOLPRO 2006.1*
111. Schmidt MW, Baldridge KK, Boatz JA, Elbert ST, Gordon MS, Jensen JH, Koseki S, Matsunaga N, Nguyen KA, Su S, Windus TL, Dupuis M, Montgomery JA (1993) *J Comput Chem* 14:1347
112. CPMD, Copyright IBM Corp 1990–2006, Copyright MPI für Festkörperforschung Stuttgart 1997–2001
113. Kresse G, Hafner J (1993) *Phys Rev B* 47:558
114. Kresse G, Furthmüller J (1996) *Phys Rev B* 54:11169
115. Choi YM, Abernathy H, Chen H-T, Lin MC, Liu M (2006) *ChemPhysChem* 7:1957
116. Wang JH, Liu M, Lin MC (2006) *Solid State Ionics* 177:939
117. Choi YM, Mebane DS, Lin MC, Liu M (2007) *Chem Mater* 19:1690
118. Lamas EJ, Balbuena PB (2006) *J Chem Theory Comput* 2:1388
119. Xu Y, Ruban AV, Mavrikakis M (2004) *J Am Chem Soc* 126:4717
120. Roques J, Anderson AB (2004) *J Electrochem Soc* 151:E340
121. Balbuena PB, Altomare D, Vadlamani N, Bingi S, Agapito LA, Seminario JM (2004) *J Phys Chem A* 108:6378
122. Wang Y, Balbuena Perla B (2005) *J Phys Chem B* 109:18902
123. Panchenko A, Koper MTM, Shubina TE, Mitchell SJ, Roduner E (2004) *J Electrochem Soc* 151:A2016
124. Jacob T, Goddard WA III (2004) *J Phys Chem B* 108:8311
125. Jacob T, Merinov BV, Goddard WA III (2004) *Chem Phys Lett* 385:374
126. Jacob T, Muller RP, Goddard WA III (2003) *J Phys Chem B* 107:9465
127. Fleig J (2003) *Annu Rev Mater Res* 33:361
128. Horita T, Yamajia K, Sakaia N, Xionga Y, Katoa T, Yokokawa H, Kawada T (2002) *J Power Sources* 106:224
129. Radhakrishnan R, Virkar AV, Singhal SC (2005) *J Electrochem Soc* 152:A927
130. Hammer B, Nørskov JK (2000) *Adv Catal* 45:71
131. Clarke S, Nekovee M, de Boer PK, Inglesfield JE (1998) *J Phys* 10:7777
132. Feibelman P (2001) *Phys Rev B* 64:125403/1
133. Hyman MP, Medlin JW (2006) *J Phys Chem B* 110:15338
134. Bogicevic A, Stromquist J, Lundqvist BI (1998) *Phys Rev B* 57:R4289

135. Eichler A, Hafner J (1997) *Phys Rev Lett* 79:4481
136. Eichler A, Mittendorfer F, Hafner J (2000) *Phys Rev B* 62:4744
137. Gland JL, Korchak VN (1978) *Surf Sci* 75:733
138. Gland JL (1980) *Surf Sci* 93:487
139. Gland JL, Sexton BA, Fisher GB (1980) *Surf Sci* 95:587
140. Li T, Balbuena PB (2003) *Chem Phys Lett* 367:439
141. Gambardella P, Sljivancanin Z, Hammer B, Blanc M, Kuhnke K, Kern K (2001) *Phys Rev Lett* 87:056103/1
142. Luntz AC, Grimblot J, Fowler DE (1989) *Phys Rev B* 39:12903
143. Nolan PD, Lutz BR, Tanake PL, Davis JE, Mullins CB (1998) *Phys Rev Lett* 81:3179
144. Nolan PD, Lutz BR, Tanake PL, Davis JE, Mullins CB (1999) *J Chem Phys* 111:3696
145. Outka DA, Stohr J, Jark W, Stevens P, Solomon J, Madix RJ (1987) *Phys Rev B* 35:4119
146. Sljivancanin Z, Hammer B (2002) *Surf Sci* 515:235
147. Wurth W, Stohr J, Feulner P, Pan X, Bauchspiess KR, Baba Y, Hudel E, Rocker G, Menzel D (1990) *Phys Rev Lett* 65:2426
148. Barth JV, Zambelli T, Wintterlin J, Schuster R, Ertl G (1997) *Phys Rev B* 55:12902
149. Gravil PA, Bird DM, White JA (1996) *Phys Rev Lett* 77:3933
150. Gravil PA, White JA, Bird DM (1996) *Surf Sci* 352:248
151. Nakatsuji H, Nakai H (1993) *J Chem Phys* 98:2423
152. Li W-X, Stampfl C, Scheffler M (2003) *Phys Rev B* 67:045408/1
153. Campbell CT (1985) *Surf Sci* 157:43
154. Raukema A, Butler DA, Box FMA, Kleyn AW (1996) *Surf Sci* 347:151
155. Salazar MR, Saravanan C, Kress JD, Redondo A (2000) *Surf Sci* 449:75
156. Sun Q, Wang Y, Fan K, Deng J (2000) *Surf Sci* 459:213
157. Vattuone L, Rocca M, Valbusa U (1994) *Surf Sci* 314:L904
158. Xu Y, Greeley J, Mavrikakis M (2005) *J Am Chem Soc* 127:12823
159. Bader RFW (1994) *Atoms in molecules—A quantum theory*. Clarendon Press, Oxford
160. Bader RFW, Beddall PM (1972) *J Chem Phys* 56:3320
161. Henkelman G, Arnaldsson A, Jonsson H (2006) *Comput Mater Sci* 36:354
162. <http://theory.cm.utexas.edu/bader/>
163. Liu Z-P, Jenkins SJ, King DA (2004) *Phys Rev Lett* 93:156102
164. Liu Z-P, Jenkins SJ, King DA (2005) *Phys Rev Lett* 94:196102
165. Fu Q, Saltsburg H, Flytzani-Stephanopoulos M (2003) *Science* 301:935
166. Guzman J, Carrettin S, Corma A (2005) *J Am Chem Soc* 127:3286
167. Nagy A, Mestl G, Ruhle T, Weinberg G, Schlögl R (1998) *J Catal* 179:548
168. Nagy AJ, Mestl G (1999) *Appl Catal A* 188:337
169. Nagy AJ, Mestl G, Herein D, Weinberg G, Kitzelmann E, Schlögl R (1999) *J Catal* 182:417
170. White MG, Beuhler RJ (2004) *J Chem Phys* 120:2445
171. Feibelman PJ, Esch S, Michely T (1996) *Phys Rev Lett* 77:2257
172. Stipe BC, Rezaei MA, Ho W, Gao S, Persson M, Lundqvist BI (1997) *Phys Rev Lett* 78:4410
173. Wintterlin J, Schuster R, Ertl G (1996) *Phys Rev Lett* 77:123
174. Norby P, Krogh AIG, Krogh Andersen E, Andersen NH (1995) *J Solid State Chem* 119:191
175. Iliev MN, Abrashev MV, Lee HG, Popov VN, Sun YY, Thomsen C, Meng RL, Chu CW (1998) *Phys Rev B* 57:2872
176. Podobedov VB, Weber A, Romero DB, Rice JP, Drew HD (1998) *Phys Rev B* 58:43
177. Pickett WE, Singh DJ (1996) *Phys Rev B* 53:1146
178. Su YS, Kaplan TA, Mahanti SD, Harrison JF (2000) *Phys Rev B* 61:1324
179. Nicastro M, Patterson CH (2002) *Phys Rev B* 65:205111/1
180. Munoz D, Harrison NM, Illas F (2004) *Phys Rev B* 69:085115/1
181. Kotomin EA, Heifets E, Maier J, Goddard WA III (2003) *Phys Chem Chem Phys* 5:4180
182. Evarestov RA, Kotomin EA, Heifets E, Maier J, Borstel G (2003) *Solid State Commun* 127:367
183. Kotomin EA, Evarestov RA, Mastrokov YA, Maier J (2005) *Phys Chem Chem Phys* 7:2346
184. Evarestov RA, Kotomin EA, Fuks D, Felsteiner J, Maier J (2004) *Appl Surf Sci* 238:457
185. Fuks D, Dorfman S, Felsteiner J, Bakaleinikov L, Gordon A, Kotomin EA (2004) *Solid State Ionics* 173:107
186. Fuks D, Bakaleinikov L, Kotomin EA, Felsteiner J, Gordon A, Evarestov RA, Gryaznov D, Maier J (2006) *Solid State Ionics* 177:217
187. Woodley SM, Catlow CRA, Gale JD, Battle PD (2000) *Chem Commun* 1879
188. Islam MS (2000) *J Mater Chem* 10:1027
189. Islam MS (2002) *Solid State Ionics* 154:75
190. Kovaleva NN, Gavartin JL, Shluger AL, Boris AV, Stoneham AM (2002) *J Exp Theor Phys* 94:178
191. Blöchl P (1994) *Phys Rev B* 17:953
192. Monkhorst HJ, Pack JD (1976) *Phys Rev B* 13:5188
193. Wang W, Zhang H-B, Lin G-D, Xiong Z-T (2000) *Appl Catal B* 24:219
194. Choi YM, Lin MC, Liu M (2007) *Angew Chem, Int Ed* 46:7214
195. Nosé S (1984) *Mol Phys* 52:255
196. Podobedov VB, Weber A, Romero DB, Rice JP, Drew HD (1998) *Solid State Commun* 105:589
197. Koep E, Compson C, Liu M, Zhou ZP (2005) *Solid State Ionics* 176:1
198. Zha S, Moore A, Abernathy H, Liu M (2004) *J Electrochem Soc* 151:A1128
199. Zha S, Rauch W, Liu M (2004) *Solid State Ionics* 166:241
200. Trovarelli A (ed) (2000) *Catalysis by ceria and related materials*. Imperial College Press, London
201. Ghosh P, Sundaram A, Venkatasubramanian V, Caruthers JM (2000) *Comput Chem Eng* 24:685
202. Holland JH (1975) *Adaptation in natural and artificial systems: An introductory analysis with applications to biology, control, and artificial intelligence*. University of Michigan Press, Ann Arbor
203. Chakraborti N (2004) *Int Mater Reviews* 49:246
204. Ho K-M, Shvartsburg AA, Pan B, Lu Z-Y, Wang C-Z, Wacker JG, Fye JL, Jarrold MF (1998) *Nature* 392:582
205. Chakraborti N, Mishra P, Erkoc S (2004) *J Phase Equilib Diffusion* 25:16
206. Klimeck G, Bowen RC, Boykin TB, Salazar-Lazaro C, Cwik TA, Stoica A (2000) *Superlattices Microstruct* 27:77
207. Deaven DM, Ho KM (1995) *Phys Rev Lett* 75:288
208. Hart GLW, Blum V, Walorski MJ, Zunger A (2005) *Nature Mater* 4:391
209. Jóhannesson G.H., Bligaard T, Ruban AV, Skriver HL, Jacobsen KW, Nørskov JK (2002) *Phys Rev Lett* 88:255506/1
210. Engstrom JR, Weinberg WH (2000) *AIChE J* 46:2
211. Koizumi H, Takeuchi I (2004) *Nature Mater* 3:429
212. Reddington E, Sapienza A, Gurau B, Viswanathan R, Saranganani S, Smotkin ES, Mallouk TE (1998) *Science* 280:1735
213. Fleischauer MD, Hatchard TD, Rockwell GP, Topple JM, Trussler S, Jericho SK, Jericho MH, Dahn JR (2003) *J Electrochem Soc* 150:A1465
214. Liu M, Winnick J (1997) *J Electrochem Soc* 144:1881
215. Han X, Zhang Y, Xu H (2003) *Chem Phys Lett* 378:269
216. Han X, Zhang Y, Xu H (2004) *J Comp Chem* 25:968
217. Reuter K, Scheffler M (2001) *Phys Rev B* 65:035406/1
218. Cortright RD, Dumesic JA (2002) *Adv Catal* 46:161
219. Laidler KJ (1987) *Chemical kinetics*. Harper and Row, New York